

## Supplementary Data

### Robust mechanical properties of $\text{Ag}_2\text{Se}_{1-x}\text{Te}_x$ thermoelectric materials

Heyang Chen<sup>1,#</sup>, Shenghong Ren<sup>2,3,#</sup>, Hengyang Feng,<sup>1</sup> Tian-Ran Wei<sup>1,4,\*</sup>, Ling Fu<sup>1</sup>,  
Zhenyu Pan<sup>1,\*</sup>, Kunpeng Zhao<sup>1,4</sup>, Xiuyan Li<sup>2</sup> & Xun Shi<sup>1,5,\*</sup>

<sup>1</sup>State Key Laboratory of Metal Matrix Composites, School of Materials Science and Engineering, Shanghai Jiao Tong University, Shanghai 200240, China

<sup>2</sup>Institute of Metal Research, Chinese Academy of Sciences, Shenyang 110016, China

<sup>3</sup>School of Materials Science and Engineering, University of Science and Technology of China, Hefei 230026, China

<sup>4</sup>Wuzhen Laboratory, Tongxiang 314500, China

<sup>5</sup>State Key Laboratory of High Performance Ceramics and Superfine Microstructures, Shanghai Institute of Ceramics, Chinese Academy of Sciences, Shanghai 200050, China

#Contributed equally to this work.

\*Corresponding authors: tianran\_wei@sjtu.edu.cn (Tian-Ran Wei); zpan@sjtu.edu.cn (Zhenyu Pan); xshi@mail.sic.ac.cn (Xun Shi)

#### 1. Calculation of modulus

The modulus can be calculated via sound speed. Shear modulus  $G$  and bulk modulus  $B$  and Young's modulus  $E$  are calculated as follows [1]:

$$B = \rho v_l^2 - \frac{4}{3}G \quad (\text{S1})$$

$$G = \frac{E}{2(1+\nu)} \quad (\text{S2})$$

$$E = \frac{\rho v_l^2 (3v_l^2 - 4v_t^2)}{v_l^2 - v_t^2} \quad (\text{S3})$$

$$\nu = \frac{1 - 2(v_t/v_l)^2}{2 - 2(v_t/v_l)^2} \quad (\text{S4})$$

where  $\rho$  is the density,  $v_l$  and  $v_t$  are longitudinal and transverse sound speed,  $\nu$  is the Poisson's ratio.

#### 2. Measurement of fracture toughness

The measurement of fracture toughness is based on the single-edge notched-bending method. The sample with dimensions of 3 mm × 2 mm × 18 mm is cut with a pre-crack of 1.1 mm depth. The fracture toughness  $K_{IC}$  can be obtained from the following equations [1]:

$$K_{IC} = \frac{FS}{BW^{3/2}} f\left(\frac{c}{W}\right) \quad (S5)$$

$$f\left(\frac{c}{W}\right) = 2.9\left(\frac{c}{W}\right)^{1/2} - 4.6\left(\frac{c}{W}\right)^{3/2} + 21.8\left(\frac{c}{W}\right)^{5/2} - 37.6\left(\frac{c}{W}\right)^{7/2} + 38.7\left(\frac{c}{W}\right)^{9/2} \quad (S6)$$

where  $F$ ,  $S$ ,  $W$ ,  $B$ , and  $c$  are breaking force, supporting span distance (12 mm), sample height (3 mm), sample width (2 mm) and crack depth (1.1 mm), respectively.

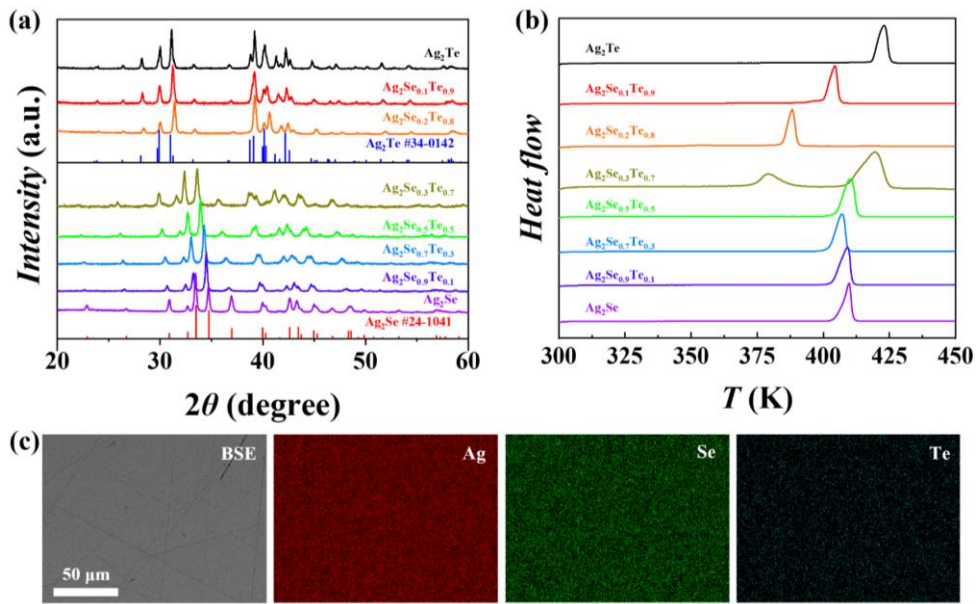


**Figure S1.** (a) Room-temperature bulk XRD patterns and (b) DSC heat flow curves for Ag<sub>2</sub>Se<sub>1-x</sub>Te<sub>x</sub> ( $x = 0, 0.1, 0.3, 0.5, 0.7, 0.9, 1$ ) samples. (c) EDS mapping of Ag, Se and Te for a typical composition, Ag<sub>2</sub>Se<sub>0.7</sub>Te<sub>0.3</sub>.

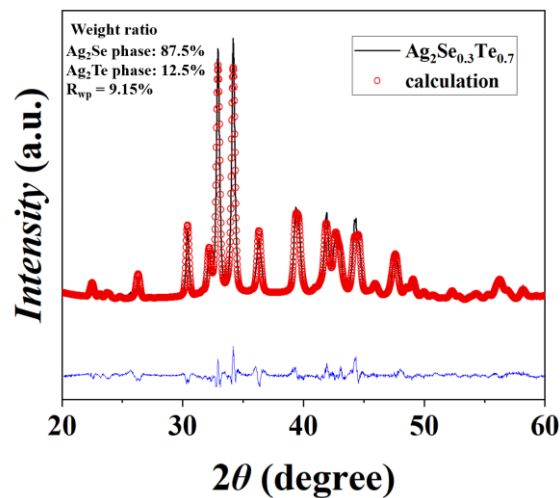


**Figure S2.** XRD refinement for Ag<sub>2</sub>Se<sub>0.3</sub>Te<sub>0.7</sub> with mixed phases.

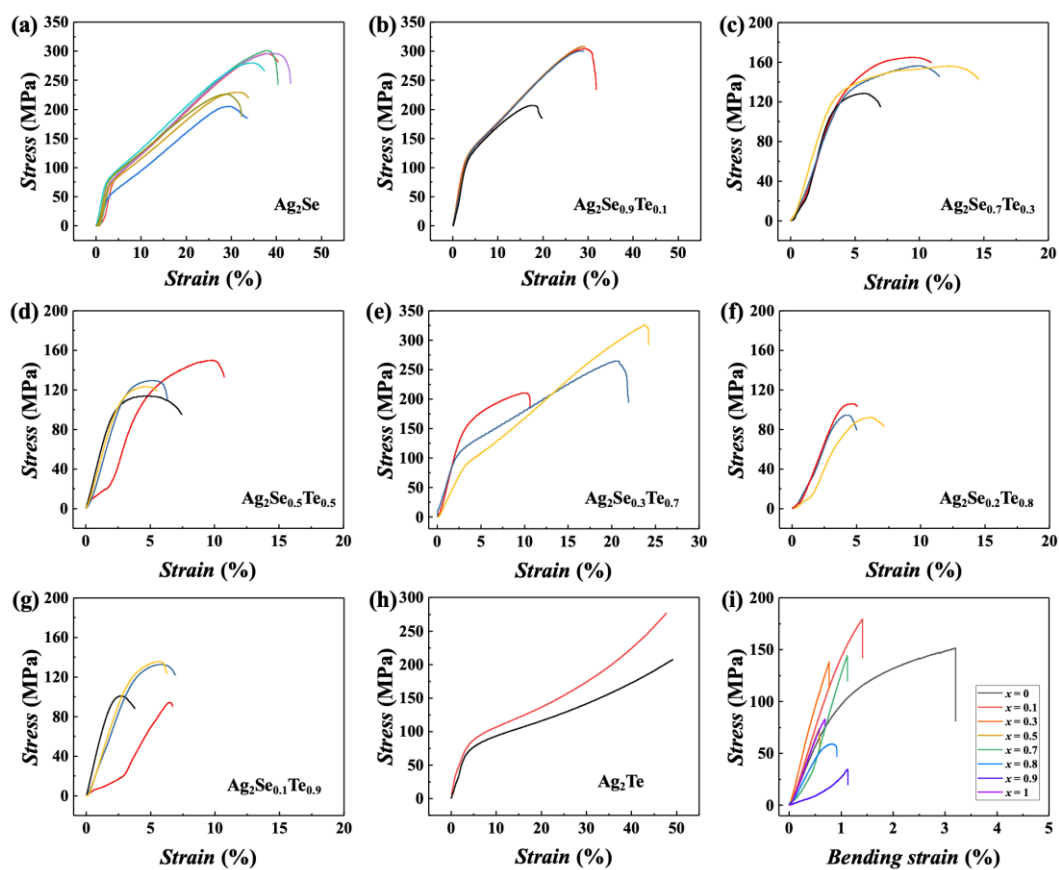


**Figure S3.** (a)-(h) Compression stress-strain curves and (i) three-point bending stress-strain curves for  $\text{Ag}_2\text{Se}_{1-x}\text{Te}_x$  samples.

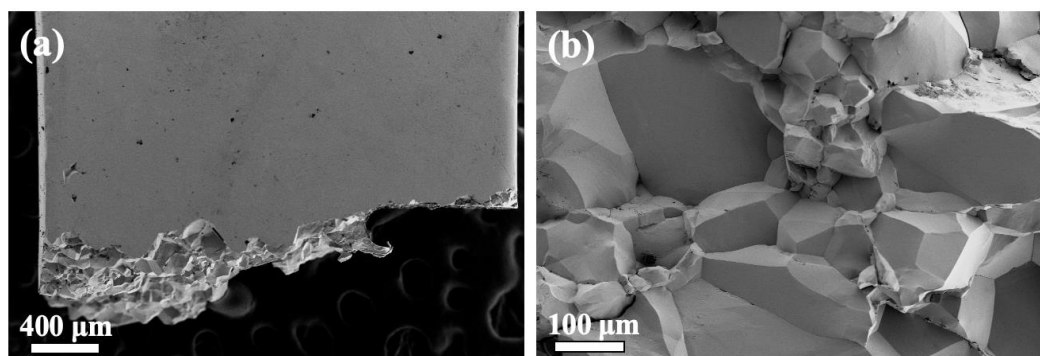


**Figure S4.** Fractured surface morphologies of bent  $\text{Ag}_2\text{Se}_{0.9}\text{Te}_{0.1}$  showing typical intergranular morphology.

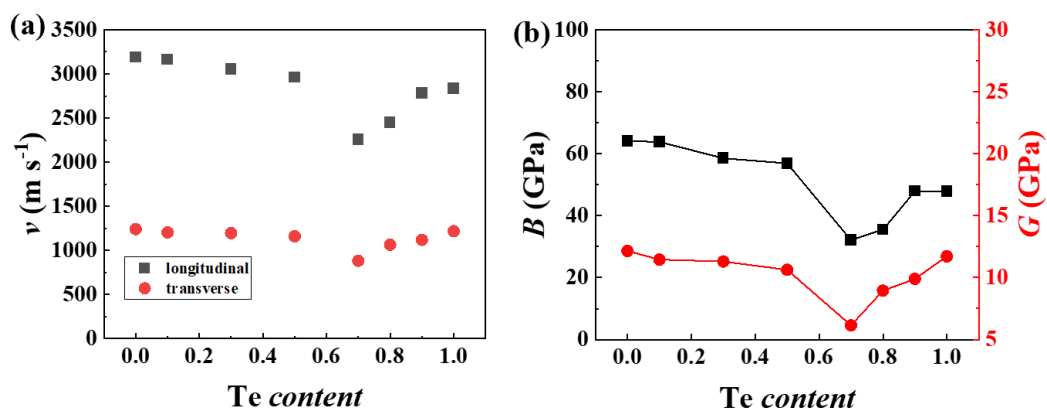


**Figure S5.** (a) Measured sound speed and (b) derived bulk modulus  $B$  and shear modulus  $G$  for  $\text{Ag}_2\text{Se}_{1-x}\text{Te}_x$  samples.

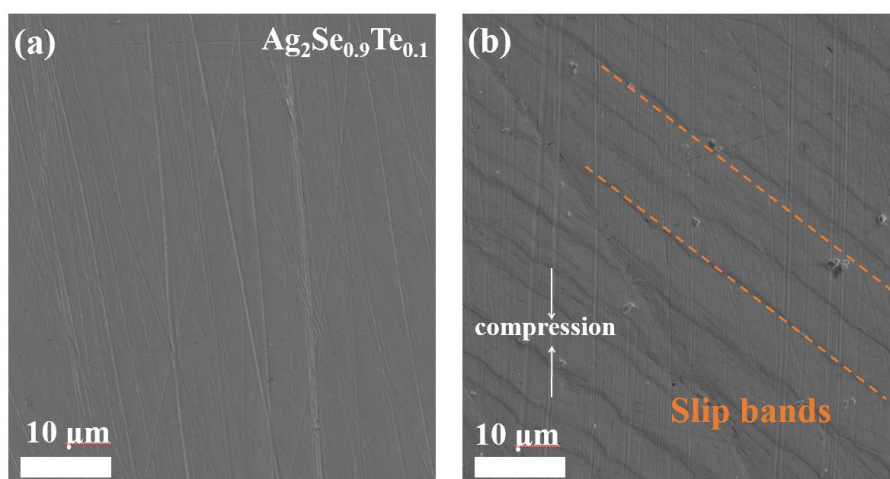


**Figure S6.** SEM images of the surfaces of  $\text{Ag}_2\text{Se}_{0.9}\text{Te}_{0.1}$  (a) before and (b) after compression (strain  $\sim 10\%$ ). Slip bands on the surface are marked.

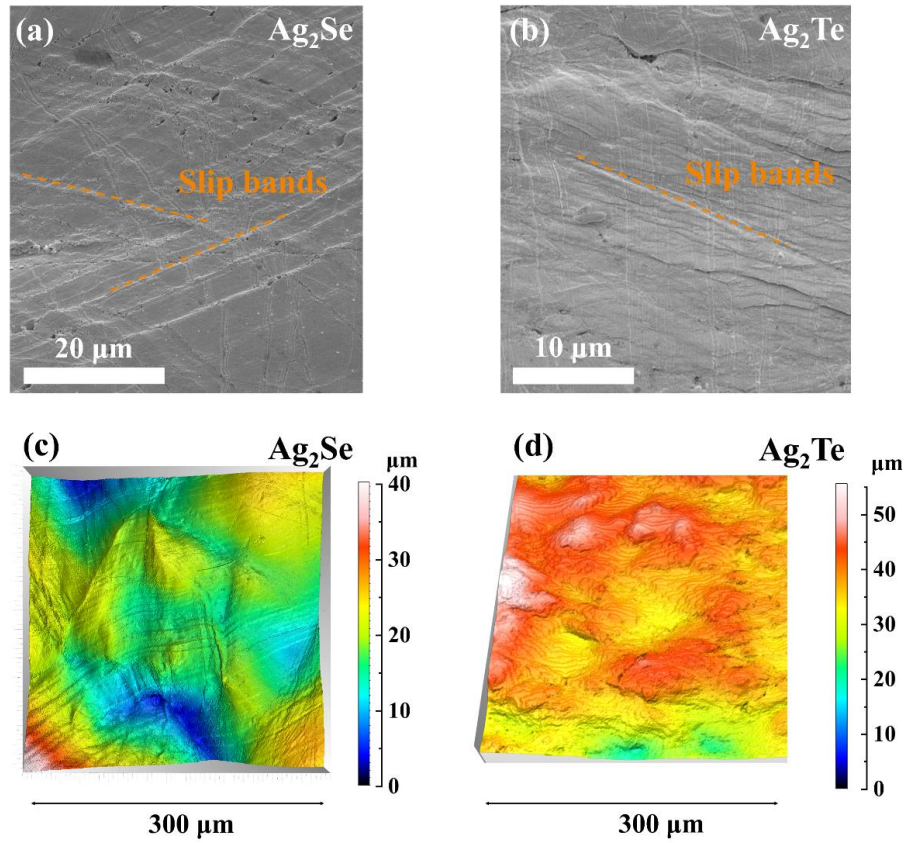


**Figure S7.** SEM images of (a) Ag<sub>2</sub>Se and (b) Ag<sub>2</sub>Te after compression. Slip bands are marked by orange dashed lines. Confocal laser scanning microscopy (CLSM) images of (c) Ag<sub>2</sub>Se and (d) Ag<sub>2</sub>Te after compression. The compression strains of Ag<sub>2</sub>Se and Ag<sub>2</sub>Te are around 30% and 50%, respectively.

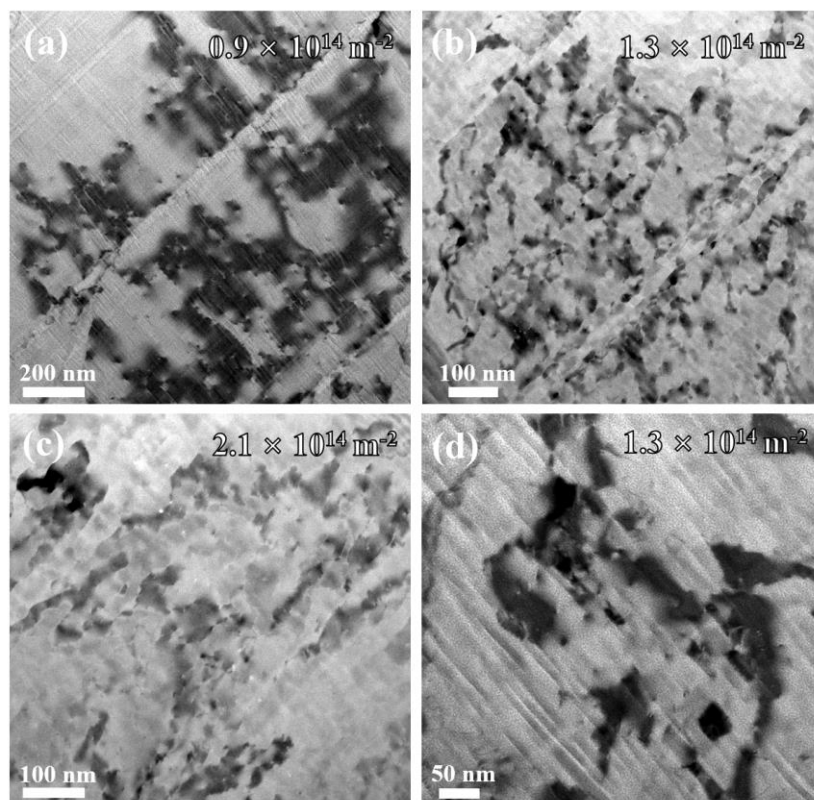


**Figure S8.** TEM bright-field images for  $\text{Ag}_2\text{Se}_{0.9}\text{Te}_{0.1}$  with compression strain of 10%. Estimated dislocation densities are marked on each panel.

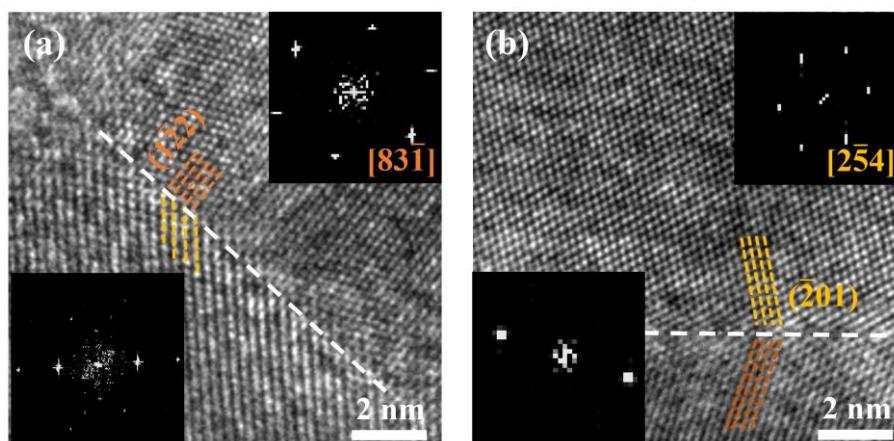


**Figure S9.** HRTEM images for  $\text{Ag}_2\text{Se}_{0.9}\text{Te}_{0.1}$  with compression strain of 10%, showing coherent or semi-coherent interfaces.

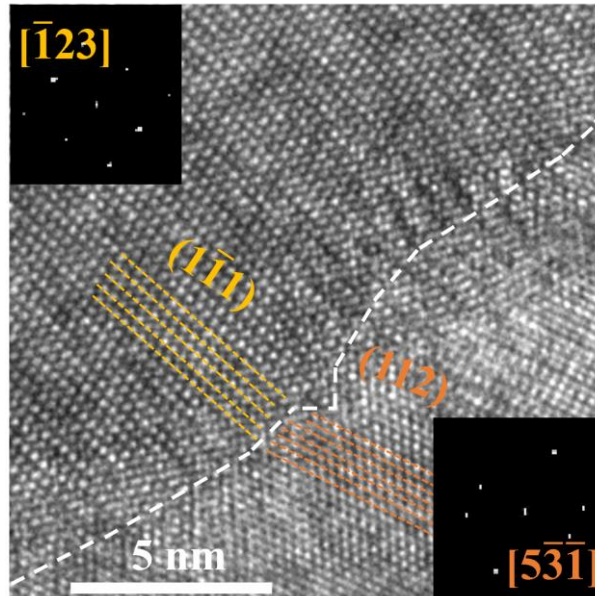


**Figure S10.** HRTEM image for  $\text{Ag}_2\text{Te}$  with compression strain of  $\sim 48\%$ , showing a semi-coherent boundary.

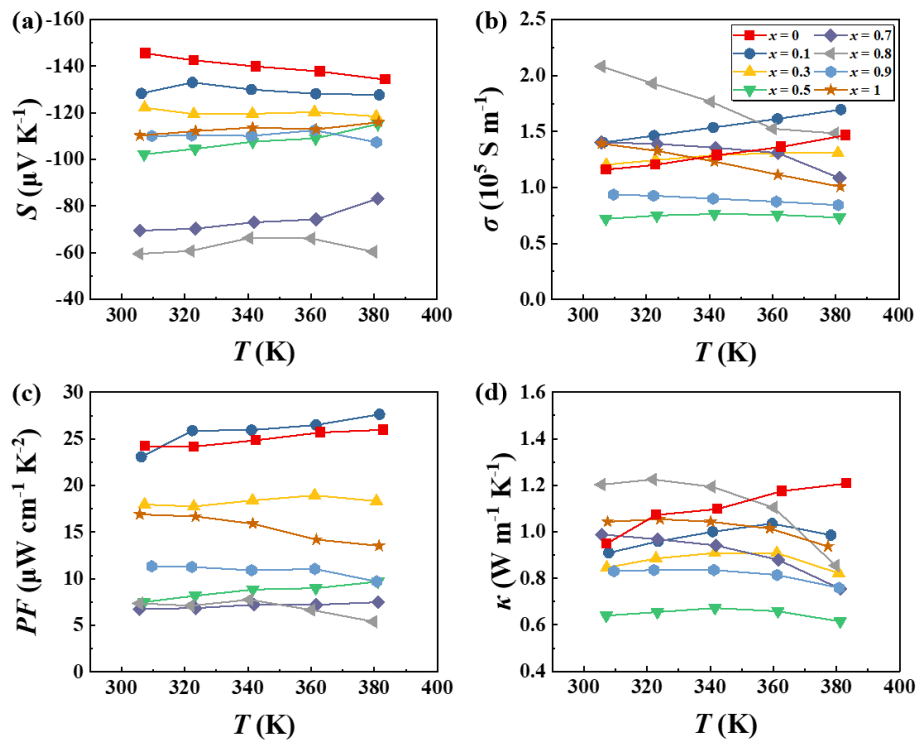


**Figure S11.** Temperature dependence of (a) Seebeck coefficient, (b) electrical conductivity, (c) power factor and (d) thermal conductivity of  $\text{Ag}_2\text{Se}_{1-x}\text{Te}_x$  with optimized Ag content.

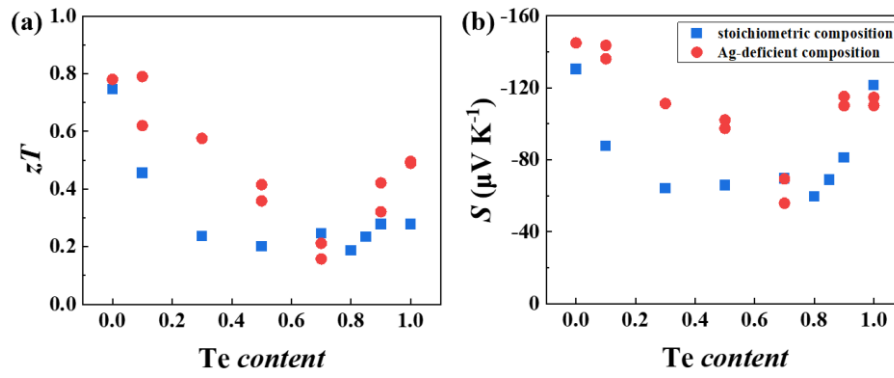


**Figure S12.** Room-temperature (a)  $zT$  value and (b) Seebeck coefficient varying with Te content for stoichiometric and Ag-deficient  $\text{Ag}_2\text{Se}_{1-x}\text{Te}_x$  samples.

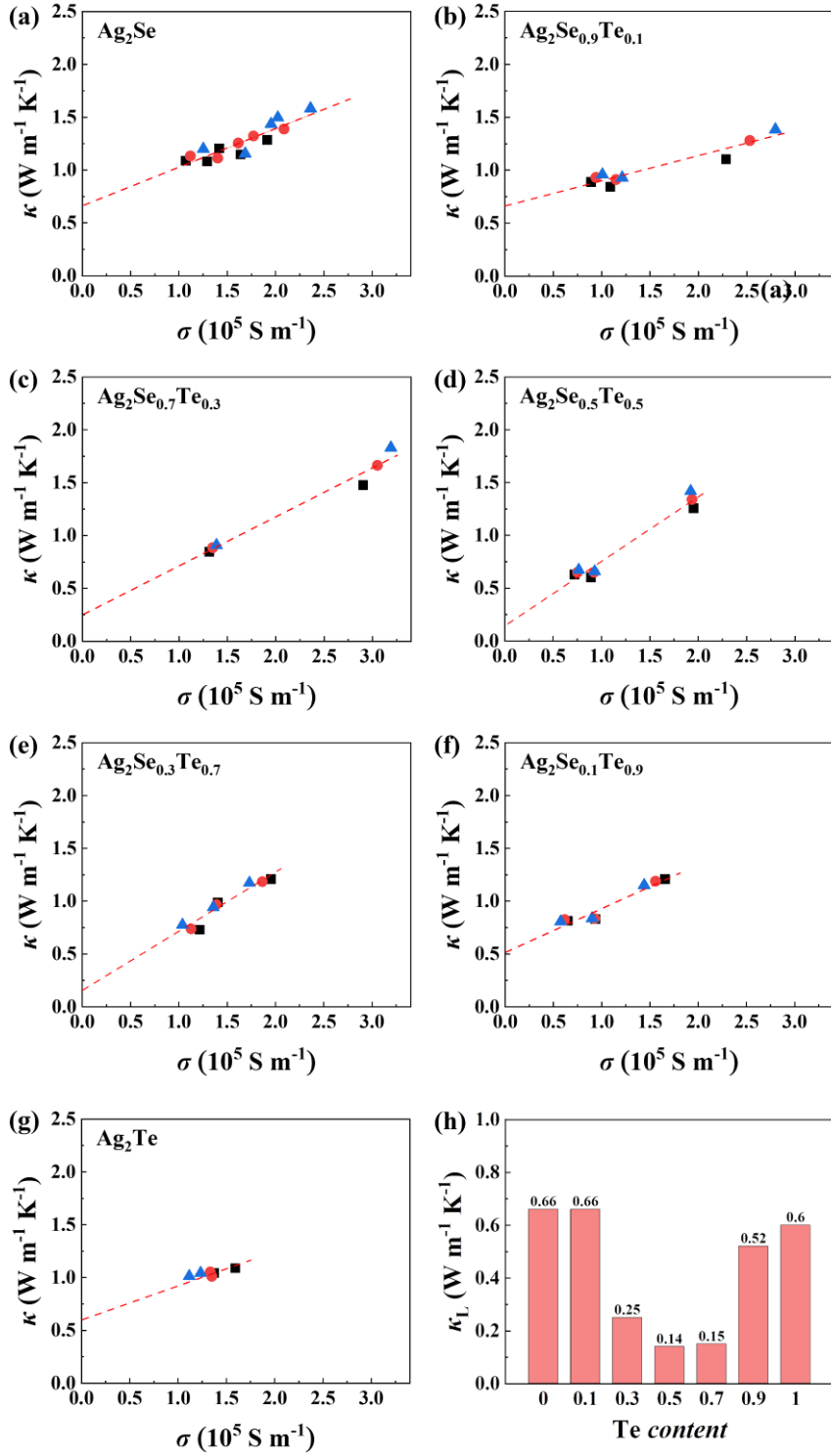


**Figure S13.** (a)-(g) The relation of electrical conductivity  $\sigma$  with thermal conductivity  $\kappa$  for  $\text{Ag}_2\text{Se}_{1-x}\text{Te}_x$  at room temperature. The red dashed line is the linear fitting of the scatters, and the intercept is estimated as the lattice thermal conductivity. (h) Room-temperature lattice thermal conductivity for  $\text{Ag}_2\text{Se}_{1-x}\text{Te}_x$  samples.

**Table S1** Ultimate compression strain and strength for  $\text{Ag}_2\text{Se}_{1-x}\text{Te}_x$  materials in this work and references. The data of  $\text{Bi}_2\text{Te}_3$ -based polycrystalline materials are included for comparison.

Composition	Compression Strain (%)	Compression Strength (MPa)	Reference
$\text{Ag}_2\text{Se}$	40	275	[2]
$\text{Ag}_2\text{Se}$	12	47	[3]
$\text{Ag}_{1.9}\text{Cu}_{0.1}\text{Se}$	19	96	[3]
$\text{Ag}_2\text{Se}/\text{CNTs}$	8	99.5	[4]
$\text{Ag}_2\text{Te}$ without domains	5.5	115	[5]
$\text{Ag}_2\text{Te}$ with domains	13-16	140-160	[5]
$\text{Ag}_2\text{Te}$	24 (20-29)	94 (81-110)	[6]
$\text{Ag}_2\text{Se}_{0.04}\text{Te}_{0.96}$	10 (4.5-25)	103 (74-128)	
$\text{Ag}_2\text{Se}_{0.08}\text{Te}_{0.92}$	10 (4-21.5)	92 (49-180)	
$\text{Ag}_2\text{Se}_{0.12}\text{Te}_{0.88}$	17 (13-20)	160 (144-170)	
$\text{Ag}_2\text{Se}_{0.16}\text{Te}_{0.92}$	14 (6-19)	127 (95-143)	
$\text{Ag}_2\text{Se}_{0.2}\text{Te}_{0.8}$	22 (15-35)	133 (90-152)	
$\text{Ag}_2\text{Se}$	34.5 (29-40)	261.7 (205-301)	This work
$\text{Ag}_2\text{Se}_{0.9}\text{Te}_{0.1}$	26.7 (20-29)	279.2 (206-308)	
$\text{Ag}_2\text{Se}_{0.7}\text{Te}_{0.3}$	9.8 (6-13)	151.0 (128-165)	
$\text{Ag}_2\text{Se}_{0.5}\text{Te}_{0.5}$	6.6 (5-10)	128.8 (112-150)	
$\text{Ag}_2\text{Se}_{0.3}\text{Te}_{0.7}$	18 (10-24)	266.7 (210-325)	
$\text{Ag}_2\text{Se}_{0.2}\text{Te}_{0.8}$	5.1 (4.3-6.3)	97.7 (92-106)	
$\text{Ag}_2\text{Se}_{0.1}\text{Te}_{0.9}$	5.3 (3-6)	115.0 (93-135)	
$\text{Ag}_2\text{Te}$	48.9 (47.8-50)	241.5 (207-276)	
$\text{Bi}_2\text{Te}_{2.7}\text{Se}_{0.3}$	4	117	[7]
$\text{Bi}_2\text{Te}_{2.9}\text{S}_{0.1}(\text{TeI}_4)_{0.0012}$	5	230	[8]
$\text{Bi}_2\text{Te}_{2.915}\text{S}_{0.1}$	3	160	[9]
$\text{Bi}_{0.399}\text{Sb}_{1.596}\text{Pb}_{0.05}\text{Te}_3$	4	200	[7]
$\text{Bi}_{0.4}\text{Sb}_{1.6}\text{Te}_{2.97}$	5	250	[10]
$\text{Bi}_{0.4}\text{Sb}_{1.6}\text{Te}_{3.72}$	2	78	[11]
$\text{Bi}_{0.5}\text{Sb}_{1.5}\text{Te}_3$	3.3	114	[12]
$\text{Bi}_{0.4}\text{Sb}_{1.6}\text{Te}_3$	2	91	[11]
$\text{Bi}_{0.4}\text{Sb}_{1.6}\text{Te}_3$	4	178	[10]
$\text{Bi}_{0.4}\text{Sb}_{1.6}\text{Te}_3$	2.5	60	[13]

## Reference

1. Green DJ. *An introduction to the mechanical properties of ceramics*. Cambridge: Cambridge University Press, 1998.
2. Liu M, Zhang X, Zhang S, Pei Y. Ag<sub>2</sub>Se as a tougher alternative to n-type Bi<sub>2</sub>Te<sub>3</sub> thermoelectrics. *Nat Commun* 2024; **15**: 6580.
3. Chen J, Sun Q, Bao D, *et al.* Simultaneously enhanced strength and plasticity of Ag<sub>2</sub>Se-based thermoelectric materials endowed by nano-twinned CuAgSe secondary phase. *Acta Mater* 2021; **220**: 117335.
4. Wang H, Liu X, Zhou Z, *et al.* Constructing n-type Ag<sub>2</sub>Se/CNTs composites toward synergistically enhanced thermoelectric and mechanical performance. *Acta Mater* 2022; **223**: 117502.
5. Wang H, Feng X, Lu Z, *et al.* Synergetic enhancement of strength–ductility and thermoelectric properties of Ag<sub>2</sub>Te by domain boundaries. *Adv Mater* 2023; **35**: 2302969.
6. Feng L, Guo A, Liu K, *et al.* Highly deformable Ag<sub>2</sub>Te<sub>1-x</sub>Se<sub>x</sub>-based thermoelectric compounds. *Mater Today Phys* 2023; **33**: 101051.
7. Sun Y, Guo F, Feng Y, *et al.* Performance boost for bismuth telluride thermoelectric generator via barrier layer based on low Young's modulus and particle sliding. *Nat Commun* 2023; **14**: 8085.
8. Zhu Y, Sun Y, Zhu J, *et al.* Mediating point defects endows n-type Bi<sub>2</sub>Te<sub>3</sub> with high thermoelectric performance and superior mechanical robustness for power generation application. *Small* 2022; **18**: 2201352.
9. Zhu Y, Jin Y, Zhu J, *et al.* Design of N-type textured Bi<sub>2</sub>Te<sub>3</sub> with robust mechanical properties for thermoelectric micro-refrigeration application. *Adv Sci* 2023; **10**: 2206395.
10. Qin H, Qu W, Zhang Y, *et al.* Nanotwins strengthening high thermoelectric performance bismuth antimony telluride alloys. *Adv Sci* 2022; **9**: 2200432.
11. Qiu J, Yan Y, Xie H, *et al.* Achieving superior performance in thermoelectric Bi<sub>0.4</sub>Sb<sub>1.6</sub>Te<sub>3.72</sub> by enhancing texture and inducing high-density line defects. *Sci China Mater* 2021; **64**: 1507–1520.
12. Zheng Y, Zhang Q, Su X, *et al.* Mechanically robust BiSbTe alloys with superior thermoelectric performance: a case study of stable hierarchical nanostructured thermoelectric materials. *Adv Energy Mater* 2015; **5**: 1401391.
13. Wang W, Sun Y, Feng Y, *et al.* High thermoelectric performance bismuth telluride prepared by cold pressing and annealing facilitating large scale application. *Mater Today Phys* 2021; **21**: 100522.